ACS APPLIED MATERIALS & INTERFACES

www.acsami.org

Research Article

Capture and Decomposition of the Nerve Agent Simulant, DMCP, Using the Zeolitic Imidazolate Framework (ZIF-8)

Amani M. Ebrahim, Anna M. Plonka, Ning Rui, Sooyeon Hwang, Wesley O. Gordon, Alex Balboa, Sanjaya D. Senanayake, and Anatoly I. Frenkel*

Cite This: *ACS Appl. Mater. Interfaces* 2020, 12, 58326−58338

Read Online

ACCESS | Metrics & More | Article Recommendations | Supporting Information

ABSTRACT: Understanding mechanisms of decontamination of chemical warfare agents (CWA) is an area of intense research aimed at developing new filtration materials to protect soldiers and civilians in case of state-sponsored or terrorist attack. In this study, we employed complementary structural, chemical, and dynamic probes and *in situ* data collection, to elucidate the complex chemistry, capture, and decomposition of the CWA simulant, dimethyl chlorophosphonate (DMCP). Our work reveals key details of the reactive adsorption of DMCP and demonstrates the versatility of zeolitic imidazolate framework (ZIF-8) as a plausible material for CWA capture and decomposition. The *in situ* synchrotron-based powder X-ray diffraction (PXRD) and pair distribution function (PDF) studies, combined with Fourier transform infrared (FT-IR) spectroscopy, X-ray photoelectron spectroscopy (XPS), zinc K-edge X-ray absorption near edge structure (XANES), and Raman spectroscopies, showed that the unique structure, chemical state, and topology of ZIF-8 enable accessibility, adsorption, and hydrolysis of DMCP into the pores and revealed the importance of linker chemistry and Zn^{2+} sites for nerve agent decomposition. DMCP decontamination and decomposition product(s) formation were observed by thermogravimetric analysis, FT-IR spectroscopy, and phosphorus (P) K-edge XANES studies. Differential PDF analysis indicated that the average structure of ZIF-8 (at the 30 Å scale) remains unchanged after DMCP dosing and provided information on the dynamics of interactions of DMCP with the ZIF-8 framework. Using *in situ* PXRD and diffuse reflectance infrared Fourier transform spectroscopy (DRIFTS), we showed that nearly 90% regeneration of the ZIF-8 structure and complete liberation of DMCP and decomposition products occur upon heating.

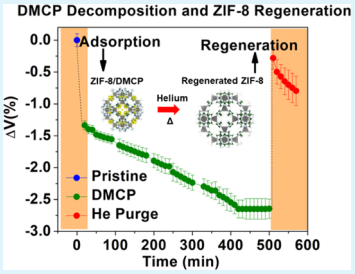

KEYWORDS: *ZIF-8, chemical warfare agents, decomposition, adsorption, regeneration, in situ multimodal*

INTRODUCTION

Chemical warfare agents (CWAs) have been a source of immense threat to humankind since their discovery and deployment in World War I.[1] Nerve agents are structurally related to organophosphate insecticides and are potent inhibitors of cell signaling pathways.[2,3] Isopropyl methylphosphonofluoridate, a G-type agent, also known as sarin and GB, is a potent organophosphorus (OP) nerve agent with a median lethal dose (LD_{50}) of 24 mg/kg.[4] G-type agents can bind to material surfaces through physical and chemical interactions.[5] Recent focus on solid reactive adsorbents has paved the route to the fundamental research of novel decontamination materials.[6,7] For example, polymers, polymer gels, textiles, metal oxides, activated carbons, covalent organic frameworks, and other hybrid materials have shown promise for the removal and decontamination of CWAs.[8−11] Studies of nerve agent chemistry and materials for their filtration and decomposition have substantially increased in laboratories by the utilization of simulants that have similar functionalities to agents but are safer and readily available with much lower acute toxicity than the live agents. Typical simulants for GB nerve agent are dimethyl methyl phosphonate (DMMP), dimethyl chlorophosphonate (DMCP), and dimethyl 4-nitrophenyl phosphate (DMNP) (Figure S1, Supporting Information, SI). Emerging studies have illustrated improved CWA decomposition through the introduction of chemical functionalities, which overcome the limitations of hydrolysis-based decomposition reactions, such as product inhibition.[12−14] A recent such study showed improved degradation of CWAs using hydrolytic nucleophilic polymers which contained nitrogen functionalities.[15] Among a wide range of materials, metal−organic frameworks (MOFs) have also gained notable interest due to their tunable porosity, diverse surface chemistry, and topology.[16−20] More specifically, aminated MOFs are being explored for CWA studies; a computational study showed that the binding energetics of DMMP are strongest on an aminated Zr-based MOF, UiO-67-NH_2, over the unmodified UiO-67.[21] These findings showcase

Received: July 18, 2020
Accepted: December 4, 2020
Published: December 17, 2020

https://dx.doi.org/10.1021/acsami.0c12985
ACS Appl. Mater. Interfaces 2020, 12, 58326−58338

the importance of multinuclearity and multifunctional materials for CWA decomposition.

Key requirements for an effective reactive adsorbent material for the removal and decomposition of CWAs include knowledge of adsorption sites, thermal and chemical stability, tunable surface chemistry and porosity, among other chemical properties.[22−26] Ongoing efforts to significantly improve decontamination technologies of adsorbent-based materials place strong emphasis on fundamental understanding of materials that can efficiently capture and decompose CWAs in ambient air. In this work, we focused on a zeolitic imidazolate framework (ZIF),[27] as a potential candidate for CWA decontamination, and explore the gas-phase chemistry of this material with CWAs by combining advanced, *in situ* characterization tools. Park et al., were the first to report the synthesis and characterization of ZIFs, in particular ZIFs (1−12).[28] ZIF-8, studied in this work, is a zeolitic type of MOF that is composed of tetrahedrally coordinated Zn^{2+} ions linked by 2-methylimidazolate (mIm) linkers with the density of the Zn atom per unit volume of 2.5/nm^3. The 1,3 positions of the two nitrogen groups in the five-membered imidazole ring are the only sites for the Zn^{2+} ions to bind to. ZIF-8 features a structure with a sodalite topology and cavities of 11.6 Å and a pore aperture of 3.4 Å in diameter where the angles between the Zn−mIm−Zn are similar to the Si−O−Si angle of 145° and the typical distance between Zn−Zn to be 6 Å (Figure 1).

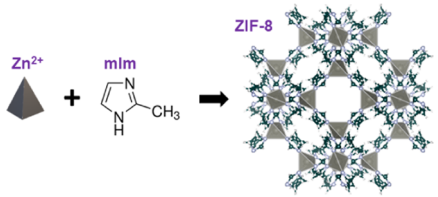

Figure 1. Representative structure of ZIF-8, formed by Zn^{2+} ions in the centers of the tetrahedra (shown in gray) and 2-methyl imidazole (mIm) linkers. N atoms are light blue and C atoms—dark green.

The connectivity of the metal−mIm−metal units results in large pore size and volume, which therefore points toward their potential usage as sorption materials.[29] Studies have shown that the high flexibility imposed by gas flow and/or high pressure cause the reorientation of the imidazolate linkers[30] that can improve diffusion of large molecules into the pore space.[31−35] Furthermore, the $-CH_3$ group attached to the linker provides hydrophobic character,[36] which can diminish the competitive nature between small polar molecules such as water vapor with other battlefield contaminants or other atmospheric gases such as CO_2 and the CWA of interest. These small molecules are known to inhibit the decomposition process.[37] The intrinsic multifunctionality of ZIF-8 can therefore provide an improved pathway for CWA capture and decontamination. As such, leveraging the nucleophilic nature of imidazole rings, not found in carboxylic-based MOFs, as well as the intrinsic hydrophobic character present, may result in improved reactive properties.

In addition to the potential utility of ZIF-8 as a sorbent, we explore its role as a catalyst for OP decomposition. The reactivity of ZIF-8 could be associated with Zn^{2+} sites (that act as Lewis acid sites in the catalytic hydrolysis of phosphate bonds) as well as the properties of the imidazole heterocycle (such as its aromatic nature, amphoteric property, and nucleophilicity) in the ZIF structure.[38] Hu et al., demonstrated using density functional theory calculations that in divalent metal complexes of Zn, Cu, or Co, the metal ion coordinates to the substrate in a monodentate fashion to facilitate the cleavage of phosphoester bonds.[39] Of the several divalent transition metal cations for phosphodiester bond hydrolysis of RNA strands, Zn^{2+}-based catalysts were more effective in the hydrolytic cleavage over other divalent cations.[40] From this study, it was determined that the Lewis sites activate the phosphate group for the nucleophilic attack *via* two mechanisms: either a ligand-assisted attack or water-assisted attack by hydroxide ions.[39] The imidazole linker can also influence the Lewis character of the metal and can directly partake in the reactions,[41,42] as revealed by a study conducted by Lambert et al., showing that the extent of proton transfer and subsequently the redox potential of Fe^{3+}/Fe^{2+} can be tuned by the protonation of the imidazole/imidazolate moieties.[43] Drawing from these studies, we thus hypothesize that the structural and chemical features of ZIF-8, along with its mononuclear Zn^{2+} sites and the slightly basic character of the mIm rings (pK_a = 8.10), provide multinuclear sites that can enable ZIF-8 to actively function as CWA decontamination material.[44−46]

Verifying this hypothesis for CWAs and their simulants is challenging. Previous gas adsorption studies conducted on ZIF-8 interacting with small molecules, such as I_2 or CO_2, indicated that the main adsorption sites are in the pore cavity, by the Zn channel sites or near the C═N, C═C bonds of the imidazolate linker,[47−50] but the reports on adsorption behavior of OP molecules, such as DMCP, have been scarce. A recent study by Ebrahimi et al., demonstrated that in the presence of nanoscale ZIFs, the half-life liquid phase hydrolysis of diazinon, an insecticide containing a thiophosphoric acid ester functionality, is reduced by a factor of 4.[51] In present study, we investigate the interaction of ZIF-8 and DMCP (approximate dimensions of DMCP molecule are shown in Figure S2, SI) at the solid−gas interface and provide a proof-of-concept for the potential application of ZIF-8 for CWA decontamination. Specifically, we employ multimodal, *in situ* approaches, developed in our prior studies of novel filtration materials for CWAs and their simulants,[37,52] to investigate the gas-phase reaction of DMCP with ZIF-8 and highlight the key features involved in the CWA decomposition process. To track the changes in the ZIF-8 framework associated with DMCP adsorption, reaction, and the regeneration processes observed in real time, we employ complimentary techniques: X-ray photoelectron spectroscopy (XPS), Raman spectroscopy, X-ray absorption spectroscopy, scanning transmission electron microscopy (STEM), *in situ* time-resolved, powder X-ray diffraction (PXRD), and pair distribution function (PDF) analysis. To detect the changes associated with the framework and DMCP decomposition and product formation, we used Fourier transform infrared (FT-IR) spectroscopy and P K-edge X-ray absorption near edge structure spectroscopy (XANES). The surface regeneration and structural reversibility of ZIF-8 are further explored using temperature-programmed desorption by diffuse reflectance infrared Fourier transform spectroscopy (DRIFTS) and *in situ* time-resolved, PXRD analysis. We reveal the effectiveness and robustness of ZIF-8 for the entrapment, adsorption, and decontamination of DMCP in the gas phase. We further explore the extent of reversibility and regeneration of the ZIF-8 framework.

https://dx.doi.org/10.1021/acsami.0c12985
ACS Appl. Mater. Interfaces 2020, 12, 58326−58338

MATERIALS AND METHODS

Dimethyl chlorophosphate (DMCP) 96% (colorless toxic liquid), methyl phosphonic acid (MPA) 98% (white solid), dimethyl methyl phosphonate (DMMP) 97% (colorless toxic liquid), 2-methyl imidazole (mIm), ZIF-8, and Zn(2-methyl imidazole)$_2$ 100% (Basolite Z1200 white fine powder) were purchased from Sigma-Aldrich. DMCP and DMMP liquids were stored in a chemical storage fridge kept at 4 °C and handled with appropriate personal protective equipment (PPE) in fume hood.

DMCP Exposure and Gravimetric Uptake. DMCP adsorption was performed at room temperature using a jar-in-jar setup.[53] The ZIF-8 powder was used as received. The exposure experiment was performed in a sealed jar that was opened to ambient air for the duration of time (approximately 30 s) needed to close the lid. There was no indication (yellow color) of DMCP hydrolysis. A schematic representation of the setup is shown in Figure S3, SI. A ceramic mortar and pestle were used to finely grind the ZIF-8 powder. ZIF-8 exposure to DMCP was performed by placing 100 mg of finely ground loose powder in a ceramic crucible pan (2.54 cm in diameter) and into a glass jar with 100 mL headspace presaturated with 500 μL of the DMCP liquid contained in a 1 mL beaker for the course of 8 h. A study showed that DMMP can diffuse through a 1 μm size ZIF-8 crystal in about 3 h.[24] Due to the relatively slow diffusion of the simulant into the pores of ZIF-8, the duration of the exposure experiment was extended to 8 h. The jar-in-jar exposure was performed in a fume hood in the Structure and Dynamics of Applied Nanomaterials (SDAN) laboratory in Chemistry Division at Brookhaven National Laboratory (BNL). The source of protons, in the jar-in-jar or *in situ* experiments, was from ambient air or He gas, respectively, each containing residual moisture. The 1−8 h DMCP-exposed samples were weighed and characterized using XPS, X-ray absorption spectroscopy (XAS), FT-IR attenuated total reflection (ATR), Raman, and STEM.

N_2 Isotherm Measurements. Nitrogen isotherm data for as-received and activated (at 120 °C for 24 h) ZIF-8 were obtained on an ASAP 2420 Micromeritic instruments at −196 °C located in the CBR filtration Branch of the U.S. Army Combat Capabilities Development Command Chemical Biological Center (CBC). Measurements on the DMCP-saturated ZIF-8 could not be run due to the sensitivity of metal diaphragm to corrosive off-gassing. The ZIF-8/DMCP (regenerated) sample was first baked at 70 °C in a gas chromatograph (GC) oven for 2 h and degassed at 120 °C for 4 h. Before nitrogen dosing, the samples were degassed under vacuum and then transferred to the N_2 dosing station. The Brunauer−Emmett−Teller (BET) surface area, S_{BET}, total pore volume, V_v and micropore volume, V_μ, (*t*-plot) were obtained from the isotherms.

Thermal Gravimetric Analysis (TGA) of Adsorbent Product(s). The thermal desorption of adsorbents and eventual decomposition on the ZIF-8 framework was determined using TGA. Measurements were performed on a PerkinElmer Pyris diamond thermogravimetric/differential thermal analysis (TG/DTA) at the Center for Functional Nanomaterials (CFN) at BNL. Samples were placed in a pretared alumina pan and heated at 10 °C/min to 800 °C under argon flow (100 mL/min).

Fourier Transform Infrared (FT-IR) Spectroscopy−Attenuated Total Reflection (ATR) Measurements. FT-IR spectra were collected on ZIF-8 and exposed ZIF-8 samples postexposure using a built-in diamond ATR bench top mode on a Thermo Scientific Nicolet iS50 FT-IR spectrometer that uses a HeNe laser and an IR source at the Chemistry Division at BNL. Prior to data collection, a background spectrum was collected before each sample spectra measurement was taken. The background and sample spectra were collected with a 4 cm^{-1} resolution with a total of 32 scans. Data collection and processing were performed using the OMNIC software.

X-ray Photoelectron Spectroscopy (XPS). Investigation of surface-bound products was performed at the Chemistry Division at BNL. ZIF-8 and ZIF-8 exposed to DMCP were pressed into a 100 mm^2 Al sheet with a load of 3 tons of pressure using a hydraulic press and holding for 5 min. The pressed plates were loaded into a SPECS ambient pressure X-ray photoelectron spectrometer (AP-XPS) instrument equipped with a PHOIBOS 150 near ambient pressure (NAP) hemispherical energy analyzer with a Mg Kα anode X-ray source. The spectra were calibrated using C (1s) peak in the CasaXPS (2.3.18) processing software. The C 1s photoemission line (adventitious carbon) at 284.8 eV was used for the calibration. The N (1s), Cl (2p), and P (2p) regions were fitted using Gaussian peak fitting, and a Shirley background subtraction was used.

Raman Spectroscopy. Raman spectra were collected on a WiTec alpha300 R combination microscope in the Center for Functional Nanomaterials at BNL using a 532 nm excitation source operating at a single spectra confocal Raman microscope configuration in back-scattering mode equipped with a motorized translation stage, charge-coupled device (CCD) detector, white illumination source, and a single-mode fiber coupled optical components with an optical resolution diffraction limit (200 nm laterally and 500 nm vertically) and a spectral resolution of 0.02 cm^{-1}. All samples were pressed into a 7 mm diameter pellet using an IR hand pellet press. Data acquisition was performed on the WiTec Control software.

Hard X-ray Absorption Spectroscopy (XAS). XANES and extended X-ray absorption fine structure (EXAFS) spectroscopies at the Zn K-edge were performed at the quick absorption spectroscopy and scattering (QAS) beamline (7-BM) at the National Synchrotron Light Source II (NSLS-II) in transmission mode. Zn K-edge was collected by scanning a Si(111) channel cut crystal monochromator energy across the absorption edge (from 200 eV below the edge through 1000 eV above the edge). Zn foil measured together with the samples was used for calibration and alignment. A total of 30 scans (at a rate of, approximately, 1 scan/min) were recorded and merged to improve the signal to noise ratio. The fresh and DMCP-exposed samples were packed into Kapton capillaries (Cole Parmer, polyimide tubing, 1.23 mm OD, 12 mm long), sealed with modeling clay on both ends and mounted onto a sample mount machine shopped at NSLS-II, which can house up to four circular pellets or four capillaries at a time. A harmonic rejection mirror (Pt coated) was used with the monochromator detuned by 30%. The ionization chambers of both the reference and transmission detectors were filled with 70% N_2 and 30% Ar. XAS data processing was performed using Demeter package 0.9.25 (Athena and Artemis).[54]

Tender Energy X-ray Absorption Spectroscopy (XAS). XANES at the P K-edge was performed at the tender energy X-ray absorption spectroscopy (TES) beamline (8-BM) at NSLS-II in a helium sample environment. P K-edge was collected by scanning a Si(111) monochromator energy across the absorption edge (from 20 eV below the edge through 50 eV above the edge). Samples and MPA standard were pressed into a 7 mm diameter pellet using an IR hand press and inserted into a typical lab-based X-ray fluorescence holder that had adhesive Kapton (1 mm thickness and 50.8 mm wide, TEKNITAPE) window on one side and a polypropylene thin film on the other side facing X-ray beam and an ultra-low-energy germanium (Ge) fluorescence detector (Canberra) positioned in the plane of beam path and 90° to sample. For the liquid DMMP and DMCP liquids, samples were prepared by mixing in aliquots of the liquid with boron nitride (<1 μm) until a paste was formed, which was then smeared onto the sample holder described above.

Scanning Transmission Electron Microscopy (STEM). High-angle annular dark-field (HAADF)-STEM micrographs and energy-dispersive X-ray spectroscopy (EDS) elemental maps of pristine ZIF-8 and ZIF-8 exposed to DMCP were taken on an aberration-corrected cold field emission electron gun Hitachi HD 2700C scanning transmission electron microscope equipped with a Bruker SDD energy-dispersive X-ray (EDX) detector operating at an accelerating voltage of 200 kV at the CFN. Samples were brushed onto a silicon nitride transmission electron microscopy (TEM) window grid (SiMpore Inc).

***In Situ* Diffuse Reflectance Infrared Fourier Transform Spectroscopy (DRIFTS).** Thermal desorption spectroscopy was collected in DRIFTS mode. The data were collected on a Thermo Scientific Nicolet iS50 FT-IR spectrometer equipped with a mercury cadmium telluride (MCT/A-narrow band—650 cm^{-1} cutoff)

https://dx.doi.org/10.1021/acsami.0c12985
ACS Appl. Mater. Interfaces 2020, 12, 58326−58338

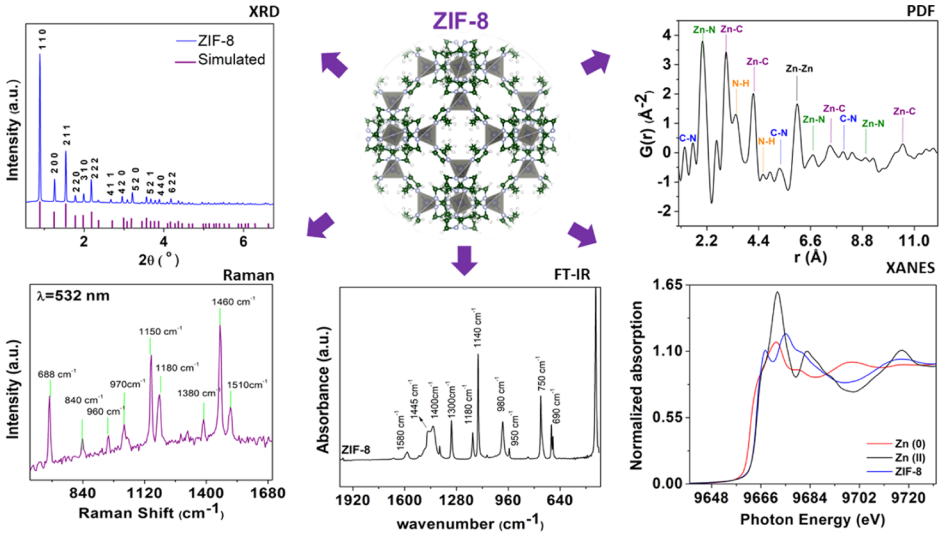

Figure 2. Complementary spectroscopic and scattering techniques for structural investigation of pristine ZIF-8. The representative structure of ZIF-8 is shown in the center. The color scheme is Zn (gray), N (blue), and C (green). From the top left corner clockwise: X-ray powder diffraction patterns for the data and simulated diffraction pattern, PDF data and peak assignment, Raman data, FT-IR spectrum of ZIF-8 and XANES spectra at the Zn K-edge for ZIF-8, and reference Zn foil and ZnO.

detector. The spectral resolution was 4 cm^{-1}. A Harrick cell in a praying mantis diffuse reflection accessory (Harrick Scientific Products) with ZnSe (15 mm) windows was used for the temperature-programmed desorption experiments. Before data collection, a KBr background at different temperatures was taken in a helium (99.99% UHP) environment with 10 mL/min flow (regulated with a four-channel Brooks Instruments mass flow controller). The temperature was ramped from 30 to 150 °C at a linear heating rate of 10 °C/min (using a Harrick Watlow EZ-Zone ATC low-voltage temperature controller). After the 30 min long equilibration at each temperature, a single-beam spectrum was collected and later used as the background. The temperature-programmed desorption (thermal desorption) experiment was performed on 20 mg of pristine and DMCP-exposed ZIF-8 samples. In the heating experiments, helium was used as a carrier gas, and the objective was to evaluate the removal of DMCP and regeneration of the ZIF-8 filter. The desorption experiment was carried out by collecting spectra for the pristine and exposed ZIF-8 after 30 min equilibration time at each temperature.

***In Situ* X-ray Diffraction (XRD) Measurements.** *In situ* measurements were carried out using a dosing unit that delivered a constant concentration of DMCP vapors to a flow cell. The dosing unit consists of a microfritted saturator (Glassblowers, Inc., NJ) that is housed in a water bath kept isothermal at 40 °C equipped with inputs and outputs to and from the flow cell. The flow cell contains the sample housed in a Kapton capillary (Cole Parmer, 1.15 mm OD) with glass wool kept on either side to prevent the sample from being displaced. The ends of the capillary were tightened with ferrules (SUPELCO, Supeltex, M-2A, 1.2 mm ID). The input of the cell was connected to a gas inlet system that carried vapors to the cell. During the experiment, the gas flow rate was fixed at 10 mL/min, and gas flow was controlled with mass flow controllers. The sample was purged with helium for 0.5 h and then exposed to DMCP with helium as the carrier gas for 8 h with a 0.5 h He purge after adsorption. During the dosing stage of the experiment, carrier gas was flowing through the saturator filled with 1 mL of DMCP liquid kept at the temperature of 40 °C. The sample was then heated to 150 °C for 1 h and cooled to room temperature. The *in situ* PXRD data were collected every minute during the dosing experiments. Powder XRD measurement diffraction data were collected at the X-ray powder diffraction (XPD) beamline (28-ID-2) of the NSLS-II, using a monochromatic beam of λ = 0.1877 Å. Diffraction data were collected in transmission mode with an amorphous silicon-based flat panel detector (PerkinElmer) mounted orthogonal to and centered on the beam path, and the two-dimensional (2D) images were integrated with the Fit2D software.[55] A Ni NIST standard was used for calibration purposes.

X-ray diffraction data analysis was performed using GSAS-II.[56] Unit cell parameters were extracted using the LeBail fitting method, where peak shapes were refined using a pseudo-Voigt function and peak asymmetry corrected by adjusting the Lorentzian contributions. The background was manually chosen using 30 points. The difference in electron density maps of the DMCP-loaded ZIF-8 was calculated using the refined model.

***In situ* Pair Distribution Function (PDF) Measurements.** *In situ* measurements were carried out following similar procedures done for the *in situ* XRD measurements using a dosing unit that delivered a constant volume of DMCP vapors to a flow cell. The sample was purged with helium for 0.5 h and then exposed to DMCP with helium as the carrier gas for 8 h with a 0.5 h helium purge after adsorption. During the dosing stage of the experiment, carrier gas was flowing through the saturator filled with 1 mL of DMCP liquid kept at the temperature of 40 °C. *In situ* atomic PDF data were obtained in 30 min frames during the whole experiment. $G(r)$ functions were obtained from the total scattering data collected at a momentum transfer, Q_{max} of 27 $Å^{-1}$ with the data processed using PDFgetX3.[57] Contributions due to adsorbent−host interactions were obtained by subtracting the DMCP-exposed ZIF-8 from the pristine ZIF-8 PDF pattern. Background scattering was subtracted from the total scattering data using an empty Kapton capillary (Cole Parmer, 1.15 mm OD). The intensities of a few select peaks highlighting the changes in the ZIF-8 local structure at 1.6, 2.0, 2.5, 3.0, 3.4, 4.2, and 6.0 Å were chosen and quantified using a Gaussian function (using Igor Pro) and were correlated with the kinetics and interactions of DMCP with the framework. Measurements were performed at the XPD beamline of the NSLS-II, using a monochromatic beam of λ = 0.1877 Å equipped with an amorphous silicon-based flat panel PerkinElmer digital imaging detector (2048 × 2048 pixel) detector (200 μm) pixel mounted orthogonal to and centered on the beam path. A Ni NIST standard was used for calibration purposes.

RESULTS AND DISCUSSION

The following section is divided into four subsections. The first subsection is dedicated to the multimodal characterization of ZIF-8. We then describe the reactive adsorption of DMCP by ZIF-8, followed by the *in situ* studies of ZIF−DMCP interaction, exploring the dynamic reaction process. In the final section, we study the structural reversibility and

https://dx.doi.org/10.1021/acsami.0c12985
ACS Appl. Mater. Interfaces 2020, 12, 58326−58338

regeneration of the ZIF-8 material with heating after DMCP exposure.

Characterization of ZIF-8. The N_2 isotherm data along with the tabulated pore structure confirm the microporous nature of ZIF-8. The detailed results are summarized in Figure S4 and Table S1. The structure of ZIF-8 is shown schematically in Figure 1 and 2. The synchrotron PXRD and atomic PDF data show the crystalline nature and long-range order of ZIF-8. The diffraction pattern shown is representative of the cubic ZIF-8 structure, with the typical diffraction peaks arising from the Bragg planes for the cubic $I\bar{4}3m$ space group.[28] The atomic pair contributions in the PDF pattern along with the different simulated atom pair correlations are indexed and show the most predominate signals in the first few peaks, which correspond to the first nearest C−N, Zn−N, and Zn−C and second Zn−N neighbors (Figure S5, SI).[48,58] The sharp peak at 6 Å corresponds to the Zn−Zn distance separated by one mIm ring (*i.e.*, Zn−mIm−Zn distance).[59−61] The collection of both IR and Raman band assignments for ZIF-8 are shown in Table S2, SI. Briefly, the Raman spectra show the mIm vibrations (Figure S6, SI).[62] The sharp band around 600 cm^{-1} represents ring puckering and out-of-plane bending vibrations. The C−H out-of-plane bend is shown around 840 and 960 cm^{-1}. The band at 1150 cm^{-1} is ascribed to C−N stretch. The band around 1180 cm^{-1} is representative of the N−H wagging mode. The band around 1300 cm^{-1} is due to methyl bend. The band around 1450 cm^{-1} is representative of the C−H wagging mode. The FT-IR spectrum for ZIF-8 (along with that for the 2-methylimidazolate linker, Figure S7, SI) provides complementary information to the Raman spectrum of mIm linker.[63,64] The bands around 1380 cm^{-1} are due to δ-CH_3. X-ray absorption spectra at Zn K-edge show that the formal oxidation state of Zn is slightly smaller than 2+, as evident by comparing the derivative of the ZIF-8 absorption coefficient with that for ZnO (Figure S8, SI).[47] In summary, the data shown in Figure 2 illustrate the high degree of order and chemical purity of this material.

Uptake, Adsorption, and Reaction of DMCP with ZIF-8. To study the adsorptive behavior of ZIF-8, we performed a gravimetric uptake study over the course of an 8 h exposure to DMCP. The gravimetric adsorption of DMCP vapors characterized by the weight gain with exposure time is presented in Figure 3a. There seem to be two distinct regions during the uptake process suggesting an induction period. Overall, the results show that there is a little DMCP uptake in a 1 h period, but the weight gain drastically increased after 8 h of exposure (~224 mg/g), which is higher than the reported adsorption capacities for activated carbon fibers. The latter are as high as 181 mg/g adsorption capacity after 100 h of DMCP exposure.[65] Only a small weight gain is observed between 300 and 400 min and then the pores saturate with DMCP molecules. The two bands in the low IR region (M−PO_x) at approximately 600 cm^{-1} are discussed in the section on IR adsorption as the vibration bands due to the formation of Zn−PO_x species. By tracking those IR vibrational bands, we found that the growth of the representative features followed the trend of DMCP uptake within ZIF-8 (Figure 3b).

Adsorption and product formation in the pores and onto the surface of porous materials like ZIF-8 can be probed using the thermal analysis method. This method can be used to extrapolate the chemical nature of the species formed. Information obtained from the weight loss pattern as well as the thermal decomposition regime for the pristine and DMCP-exposed ZIF-8 provide an estimate of the quantity of adsorbed species either formed during the adsorption process or the species likely to have degraded thermally (Figure S9, SI). A typical weight loss thermal pattern for ZIF-8 is shown. Framework decomposition by the carbonization of the methyl imidazole linker starts at 250−400 °C. The second weight loss that occurs at around 600 °C is due to the aromatization of the linkers and their subsequent decomposition. Weight loss patterns of the DMCP-exposed ZIF-8 reveal specific details: there is an initial onset of weight loss below 200 °C, suggesting that weakly adsorbed DMCP molecules are released at this temperature. Following this initial weight loss plateau, two transitions occur: one between 200 and 400 °C and one between 400 and 600 °C. The further heating and release of DMCP cause this decrease in weight loss with the evolution of the decomposed products around 400 °C, either due to thermal decomposition or due to the desorption of already decomposed surface products. The differences in the weight loss patterns illustrate the favorable molecular adsorption and decomposition of DMCP on ZIF-8.

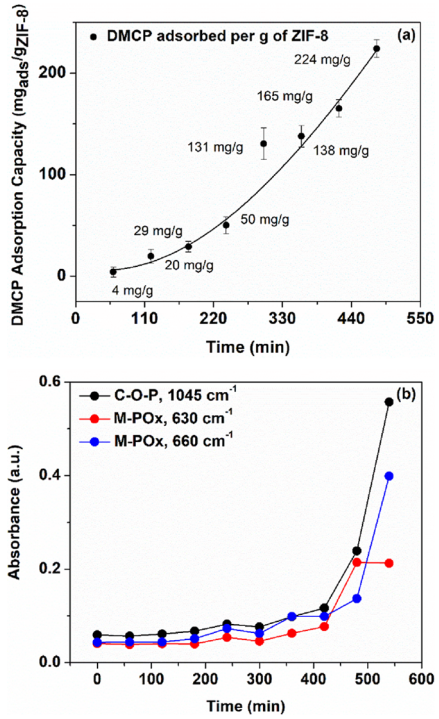

Figure 3. Uptake of DMCP within ZIF-8 framework; (a) Weight uptakes of ZIF-8 after 500 min of DMCP exposure represented as adsorption capacities. (b) Probing DMCP adsorption and MPA formation as observed by IR. Tracking the growth of DMCP features by the increase in absorbance of the C−O−P and M−PO_x vibration bands with time on ZIF-8 using the maximum peak value at the respective band after background subtraction.

To track the changes due to the reactive adsorption process, we employed several spectroscopic and scattering techniques that highlight the involvement of Zn^{2+} metal ions and imidazolate ring. We investigated DMCP adsorption using FT-IR spectroscopy. New bands appear throughout the entire IR spectrum and grow in intensity over the course of the 8 h exposure to DMCP (Figures 4 and S10). Because of the overlap between the modes arising due to ZIF-8 and ZIF-8/DMCP, we used difference spectra (with ZIF-8 as a reference) that showed the vibrations due to DMCP adsorption and

https://dx.doi.org/10.1021/acsami.0c12985
ACS Appl. Mater. Interfaces 2020, 12, 58326−58338

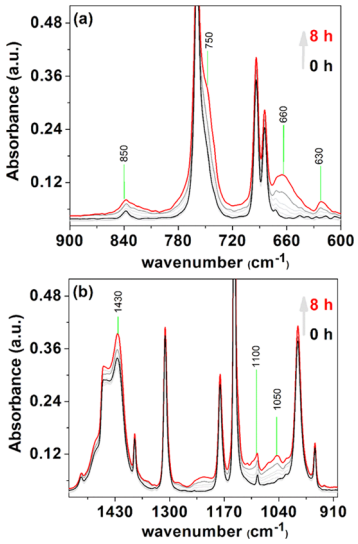

Figure 4. FT-IR spectra in the low(a) and -mid (b) IR region for ZIF-8 before (black) and after 8 h DMCP adsorption (red) showing the growth of the bands responsible for DMCP adsorption and product formation over the course of 8 h.

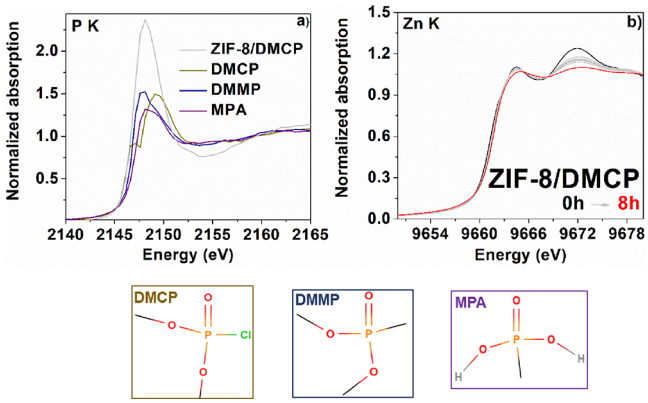

Figure 5. (a) P K-edge XANES spectra for DMMP, DMCP, MPA and ZIF-8, exposed to 8 h DMCP. (b) Normalized absorption coefficients of the XANES region at the Zn K-edge for ZIF-8 for 8 h exposure to DMCP. The starting spectrum (black) corresponds to ZIF-8; the final spectra (red) corresponds to an 8 h batch exposure to DMCP vapors. The grey curves were measured at 1 h intervals. Bottom panel shows the chemical structures of DMCP, DMMP and MPA.

hydrolysis product formation with DMCP exposure (Figure S11, SI). Positive features in the difference spectra related to DMCP adsorption and hydrolysis product formation appear over the course of DMCP exposure.[66] Considering that the main hydrolysis product for DMMP has a P−CH_3 bond (not present in DMCP) and the fact that possible DMCP products are phosphoric acid (O═P−$(OH)_3$), methyl chlorophosphate (O═P(−H)($-OCH_3$)−(Cl)) or dimethyl hydroxyphosphate (the Cl on DMCP is replaced with an OH), we use this knowledge from prior OP decomposition studies on DMMP[29,30,57] simulant to guide the band assignments for the similar moieties present in the DMCP hydrolysis products. The band assignments for gas-phase DMCP,[53] DMMP hydrolysis product (MPA), and ZIF-8/DMCP are tabulated in Table S3, SI. Two new bands associated with zinc-phosphonate structures appear at 630 and 660 cm^{-1} after exposure to DMCP.[67] These bands are likely due to the interactions of ZIF-8 with DMCP and the localization of the phosphonate moiety with Zn^{2+}. DMCP adsorption on 2-methyl imidazole was also performed, and the growth of DMCP-related spectral features was observed as a result of interaction of DMCP with mIm (Figure S12, SI). Raman spectroscopy showed that, during the time of experiment, no significant changes were observed when exposed to DMCP, suggesting that the structural integrity and crystalline nature of ZIF-8 was preserved (Figure S13, SI).

To further highlight the interactions of DMCP with ZIF-8, the speciation of phosphorus was investigated using XANES spectroscopy at the P K-edge (Figure 5a). The P K-edge XANES spectra for OP standards DMCP, DMMP, and MPA, which have unique bonding configuration around the P atom, are shown; we observe that as the type of the electron-withdrawing substituent changes and oxygen species increases, there is a linear upward shift in the edge position; *i.e.*, MPA, which has P bonded to three oxygen atoms and two hydroxyl groups, is most shifted to the right. Here, the P K-edge XANES spectrum for DMCP shows a pre-edge feature, which was not present when ZIF-8 was exposed to DMCP. By comparing the DMCP−ZIF-8 spectrum with those for pure DMCP and MPA, a representative DMCP decomposition product, a broadening of the DMCP−ZIF-8 spectrum becomes apparent, suggesting that a mixture of both molecularly adsorbed DMCP and the decomposed species coexist in the exposed ZIF-8. We also utilized Zn K-edge XANES to understand the role of Zn^{2+} during the decomposition product. Examination of the *ex situ* XANES spectra at the Zn K-edge shows subtle changes when the ZIF is exposed to DMCP (Figure 5b). Overall, the response of Zn to DMCP adsorption is small, which we attribute to the fact that not all Zn sites are equivalent and not all Zn sites interact with DMCP. These results show that DMCP adsorption is accompanied by the perturbation of Zn^{2+} ions in the ZIF-8 structure that correlates with the formation of phosphorus species as evident from FT-IR and P K-edge XANES spectroscopies.

Further investigations of DMCP−ZIF-8 surface interactions were performed using X-ray photoelectron spectroscopy (XPS). Typical peaks representative of ZIF-8 are present (Figure 6). The broad peak in the C (1s) spectrum is attributed to C═N/C═C, C−H/C−C peaks along with the Zn LMM peak. The broad N (1s) peak is ascribed to the convolution of three different species (N−Zn/N−H, N−C, N═C).[68] The two peaks in the Zn (2p) spectrum are assigned to Zn $2p_{3/2}$ and Zn $2p_{1/2}$.[68] The surface chemistry of bound species probed by XPS shows distinct features that arise due to DMCP adsorption. In the Zn (2p), a subtle shift (by −1.07 eV) toward lower binding energies is observed after DMCP adsorption. These changes are attributed to the involvement of Zn^{2+} sites in the DMCP decomposition process. A 60% decrease in the intensity of the N (1s) spectrum shown after DMCP adsorption suggests the direct involvement of nitrogen functionalities of the imidazolate linker in the decomposition process. Furthermore, the C (1s) shows notable changes upon exposure to DMCP; there is a decrease in the atomic concentration of C on the surface (Table S4, SI). Based on this change, we postulate that C in the imidazole interacts with DMCP. The Cl (2p) spectrum shows the appearance of a broad feature with a peak at approximately 198 eV, which corresponds to surface-bound chloride species possibly methyl chlorophosphate (O═P(−H)($-OCH_3$)−(Cl)) and shoulder

https://dx.doi.org/10.1021/acsami.0c12985
ACS Appl. Mater. Interfaces 2020, 12, 58326−58338

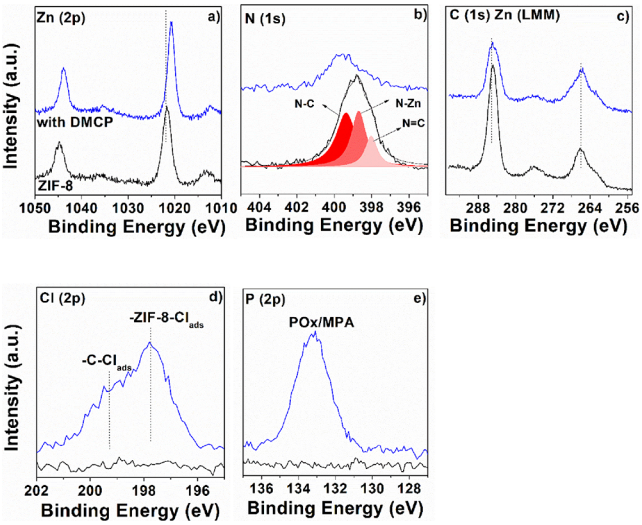

Figure 6. XPS Spectra of pristine ZIF-8 (black) and ZIF-8 exposed to DMCP (blue) at the (a) Zn (2p), (b) N (1s), (c) C (1s), Zn LMM, (d) Cl (2p) and (e) P (2p). Dashed lines in a) and c) are guides to the eye.

at approximately 199 eV, which we assign to the molecularly bound DMCP. A broad feature in the P (2p) spectrum, previously observed on Zr-polyoxometalates (POMs) and ascribed to adsorbed PO_x species, is observed.[53] The collective change and emergence of new features in the XPS spectra with DMCP exposure confirm the reactive adsorption and decomposition of DMCP.

To determine ZIF-8 morphology before and after DMCP exposure, we utilized HAADF-STEM–EDS. The images and the elemental dispersion of C, N, Zn, O, and P collected from a representative area are shown in Figure 7. The cubelike crystals of ZIF-8, remain unaffected after exposure to DMCP. The EDS maps indicate that P and O are present on the surface of ZIF-8, suggesting that there are surface-driven reactions involved between DMCP and ZIF-8.

Time-Resolved Interactions of DMCP with ZIF-8. To extract time-resolved structural information, we employed synchrotron X-ray diffraction and PDF measurements. First, we investigated the "onset" of structural changes due to DMCP using *in situ* XRD (Figure 8). Initial changes in the diffraction

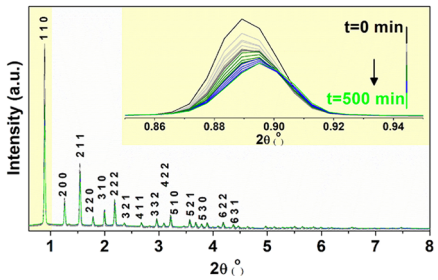

Figure 8. *In situ* time resolved PXRD data collected during the room temperature 8 h DMCP exposure. The inset highlights the changes in the first Bragg peak region.

patterns suggest the slow adsorption of DMCP into the pore space of ZIF-8. The intensities of the main Bragg reflections at low 2θ angles (high d-spacing) in a crystalline material such as ZIF-8 (which provide the sensitivity to chemical heterogeneities within the structure) drop after 180 min and gradually plateau after. Because of the larger Debye–Waller factor of sorbed molecules and the faster drop off in relative scattering power compared to the framework, the diffusion and adsorption of DMCP into the pore space is readily seen. A shift to higher 2θ angles indicates the contraction of the lattice. Further examination of PXRD patterns shows that there are structural changes during exposure; some peaks at (d_{220} and d_{310}) increase indicating the addition of sorbed atoms into those lattice planes. Using the LeBail analysis, we determined that the cell volume contracts with DMCP dosing (Figures S14

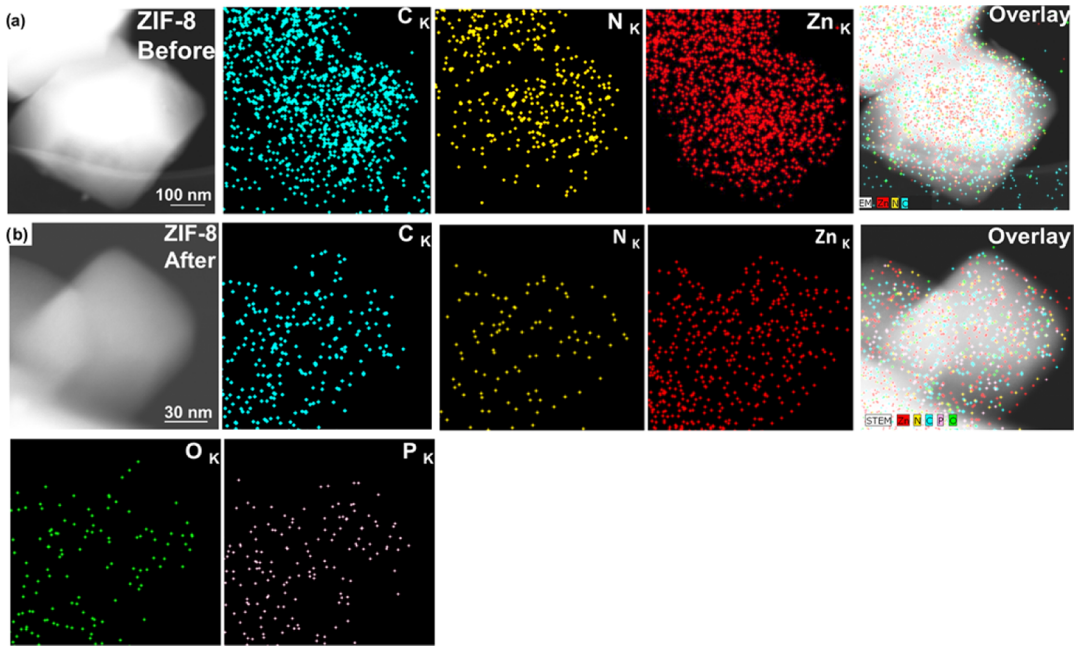

Figure 7. HAADF-STEM images and EDS elemental maps for (a) ZIF-8 before and (b) after exposure to 8 h of DMCP. Elemental composition maps of ZIF-8 shown for C, N, and Zn before and after DMCP exposure with O and P elemental maps for ZIF-8 after DMCP exposure.

https://dx.doi.org/10.1021/acsami.0c12985
ACS Appl. Mater. Interfaces 2020, 12, 58326–58338

and S15). There is about a 3% drop in cell volume with DMCP exposure from 4991 to 4859 Å^3 (Table 1 and Figure S16). This

Table 1. Unit Cell Parameters for ZIF-8 ($I\bar{4}3m$) and DMCP-Saturated ZIF-8

sample	*a*, lattice parameter (Å)	cell volume (Å^3)
ZIF-8	17.09(1)	4991(1)
ZIF-8 DMCP	16.94(2)	4859(2)

phenomenon is a result of the strong interaction of DMCP with the framework, which ultimately leads to framework contraction. The unit cell contraction occurs over the course of DMCP exposure with the most abrupt change in the first 50 min of DMCP exposure (Figure S16, SI). Analyses of the empty and DMCP-loaded ZIF-8 show that the highest electron density originates in the pores and in the vicinity of the closest six-membered ring (6MR) gate as well as near the Zn^{2+} sites (Figure 9), where adsorbed DMCP molecules are located.

Analysis of the contributions from the crystalline and amorphous components of the ZIF-8 structure with DMCP dosing was performed using *in situ* PDF, which is motivated to complement X-ray diffraction measurements. The weighted histograms of atom−atom correlations and bond distances within ZIF-8 are shown (Figure 10a,b). The full scale of PDF patterns up to 30 Å is presented in Figure S17, SI. By applying a differential PDF approach and subtracting contributions arising from framework atoms, the effect of DMCP loading can be evaluated and DMCP−ZIF-8 framework interactions can be determined (Figure 10c,d). During the dosing, we observed the largest changes in the short-range structure of ZIF-8. We did not observe the formation of new peaks in PDF; most probably the signal from loaded DMCP molecules was weaker than that of the well-ordered framework. Overall, the ZIF-8 local structure remains unchanged when dosed with DMCP. The most notable changes in relative intensities reveal those framework bonds that are most sensitive to DMCP perturbations. The intra- and intercage correlations change with DMCP exposure and the changes in $G(r)$ intensities reflect the different residence times DMCP interacts with different ZIF-8 units. The major observed change is the loss of intensity of the atom pairs that involve Zn, which can be interpreted as a disorder at the metal nodes and in turn suggests that DMCP primarily adsorbs at those sites.

The time-resolved kinetics of adsorption under DMCP dosing in different regimes reveal qualitatively the abundance of different DMCP-framework correlations (Figure 11). To evaluate time dependence of the DMCP-induced disorder in the ZIF-8 framework, we studied the peak intensity changes with time. The intensity of the peaks varies with correlation length and shows that for larger or smaller correlations, the intensity changes plateau quickly, whereas with intermediate correlations, there is an induction period and ultimately curve flattening occurs. The fastest changes in intensity occur at 6.0 Å, which is the distance between Zn−Zn in ZIF-8. This change suggests that there is a direct bonding of DMCP with the Zn sites. The trend is different at a radial distance of 3.4 Å, which are the bonds that connect the pores which form the 6MR windows. In this region, uptake is gradual and quickly reaches saturation after 100 min of continuous DMCP dosing. Strong pair−pair correlations observed at 3.0 and 2.0 Å, which are representative of the Zn−C and Zn−N interatomic distances between the metal site and the linker units, rise after 100 min of exposure and gradually saturate at 480 min. This trend suggests that there are dynamic changes to the linker moieties to accommodate DMCP molecules. In summary, the time-resolved differential PDF data reveals information on the pore dynamics with DMCP interactions. Our findings show that the pore volume is quickly filled, the nitrogen and carbon atoms of imidazole partake in the reaction, and DMCP first adsorbs into the pore window and then into the pore cavity. The intensity drop in the $G(r)$ function shows that there is a dynamic change in the correlation length of the bonds, which suggests pore shrinkage, in agreement with PXRD unit cell changes.

Surface Regeneration and Structural Reversibility of ZIF-8. The regeneration of active sites and structural reversibility were investigated using a combination of *in situ* temperature-programmed DRIFTS and *in situ* time-resolved PXRD. The liberation of DMCP from the ZIF-8 surface was investigated using temperature-programed desorption experiments in DRIFTS. The disappearance of main vibrational bands, due to molecular DMCP adsorption, upon heating indicated the complete removal of surface-bound DMCP and results in a free ZIF-8 surface (Figures S18 and 12a). Collection of the IR spectra over these temperature ranges provides insight into the DMCP/surface-bound desorption kinetics. By employing an Arrhenius plot, the desorption energy was found to be 25.4 kJ/mol (Figure 12b), which is almost half the reported value for the energetics of DMCP (P═O moiety) desorption on the surface of a monolayer coverage on amorphous silica.[69,70] These results show that ZIF-8 can readily release phosphorus bound species.

Based on the cumulative results of IR and XPS experiments, we provide a simple mechanism to demonstrate the adsorption (eqs 1 and 2) and desorption (eqs 3−5) processes (Figure 13).

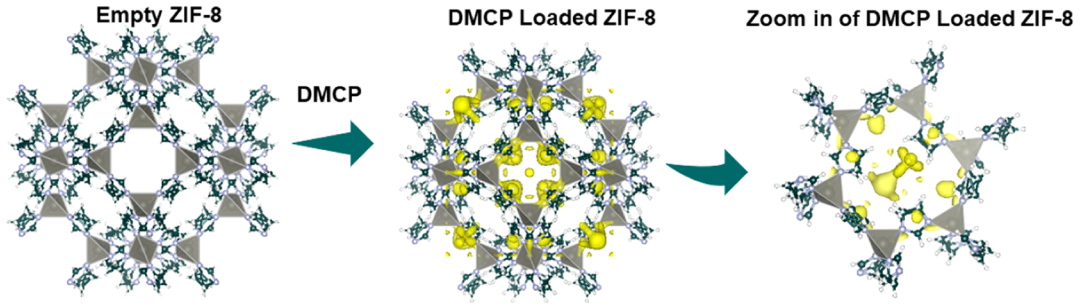

Figure 9. Difference Fourier electron density map of ZIF-8 after DMCP dosing. Electron density isosurface, drawn at 0.3 $\bar{e}$/Å^3 (yellow). The electron density distribution shows the possible locations of DMCP molecules or reaction product distribution in the pore space, by the linkers and by the Zn^{2+} metal ion. Zn is shown in gray, C—light blue, N—dark green, and H—white.

https://dx.doi.org/10.1021/acsami.0c12985
ACS Appl. Mater. Interfaces 2020, 12, 58326−58338

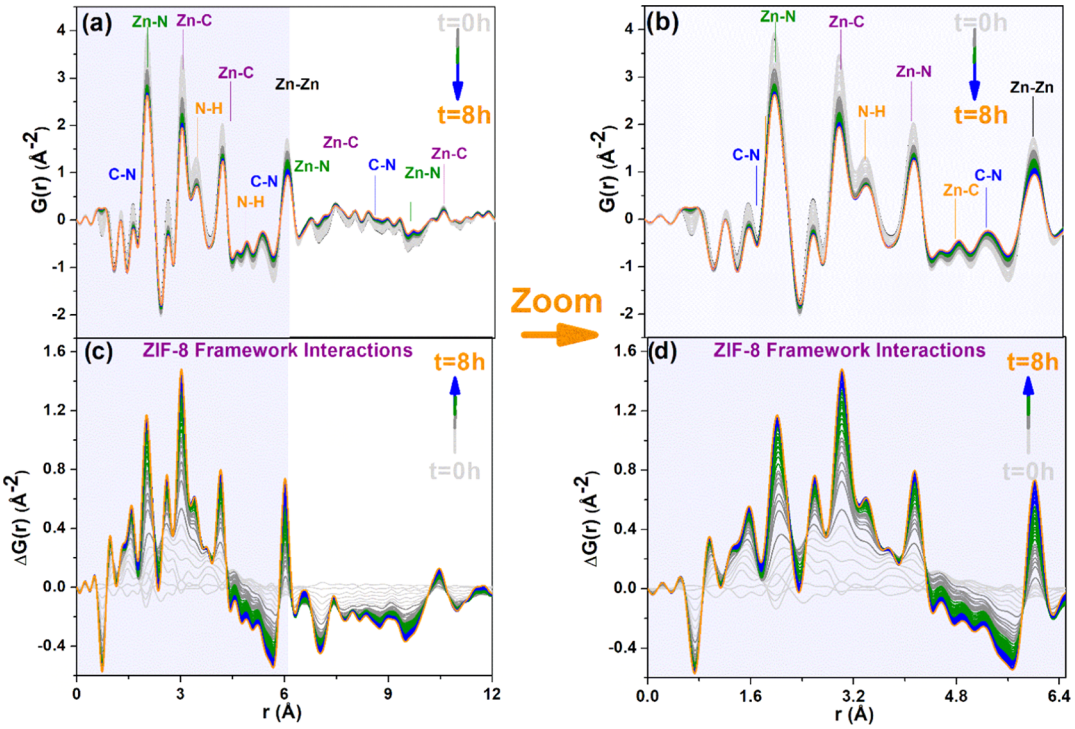

Figure 10. From the top left corner clockwise: (a) *in situ* time-resolved atomic PDF collected during DMCP adsorption, peak assignments are obtained by simulated $G(r)$ for pair-wise atoms (b) with a zoom of the region between 0 and 6 Å. The bonds ascribed to specific atomic PDFs are those with the most significant changes. (c) Differential time-resolved PDF using empty ZIF-8 and (d) subtracting from ZIF-8 undergoing DMCP adsorption with a zoom of the region between 0 and 6.0 Å. Time progresses from gray to blue and finally to orange.

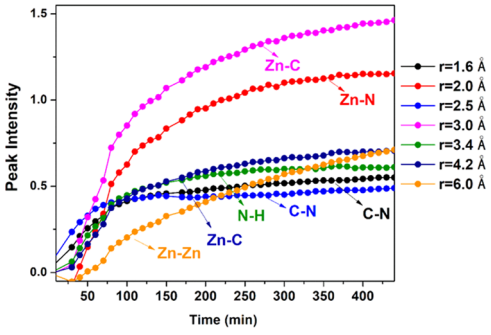

Figure 11. Evolution of different DMCP−ZIF-8 interactions (in the 6.0 Å regime) with DMCP dosing extracted from the differential PDF plots.

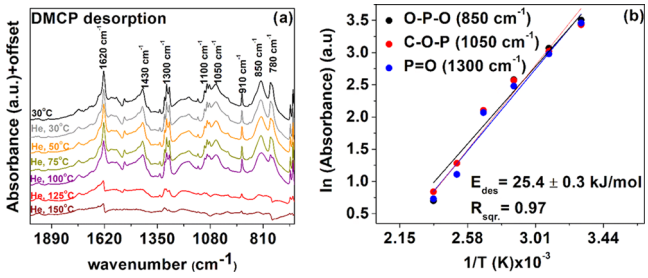

Figure 12. Regeneration of ZIF-8 sites: (a) Thermal programmed desorption DRIFTS of ZIF-8 saturated with DMCP heated from 30 to 150 °C under helium (He) flow. KBr is used as the background at the respective temperatures. The identified bands are due to DMCP adsorption. The thermal desorption spectra show that upon heating the vibrational bands begin to disappear and are fully removed after 125 °C, which shows that bound DMCP molecules are removed. (b) Arrhenius-type plot for the desorption of DMCP/products over ZIF-8 at different temperatures for three different vibrational modes representative of O−P−O, C−O−P, and P═O bands, where the background-corrected intensities are plotted against temperature and the slope of the graph providing information on the desorption energy (E_{des}) derived from (a).

The adsorption of DMCP onto ZIF-8 affords adsorbed DMCP molecules and surface products in the form of adsorbed PO_x and Cl_x species, which begin to desorb at temperatures higher than 125 °C. In the event that surface-bound Cl that desorbs above 125 °C is released as a gas; it can be a detrimental part of the decontamination process.

The N_2 isotherm experiments indicate that ZIF-8 retains its microporous structure and that DMCP adsorption occurs in the pores and on the surface of ZIF-8. The thermally treated ZIF-8/DMCP shows a 30% decrease in the volume of micropores and a 35% decrease in surface area (Figure S19 and Table S5, SI). These results suggest that the interactions of ZIF-8/DMCP are in the pores and on the surface, in agreement with the PXRD and PDF results (*vide supra*). Furthermore, the isotherm measurements help provide additional evidence of the surface regeneration after the exposure as described below.

With the purpose of assessing the framework regeneration, a time-resolved *in situ* X-ray diffraction study was performed after prolonged exposure to DMCP. We note that the evacuation of the pores leads to the increase of the intensity of the peaks that were before stunted due to disperse electron density from molecules inside the pores. As such, those peak height changes are a secondary proof of the successful evacuation of the pore space. Following DMCP dosing, the system was flushed and heated at 150 °C in a helium environment. After this treatment, an increase in the intensity

https://dx.doi.org/10.1021/acsami.0c12985
ACS Appl. Mater. Interfaces 2020, 12, 58326−58338

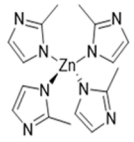

(1) $(CH_3O)_2POCl$ (g) ⟶ $(CH_3O)_2POCl$ (ads)

(2) $(CH_3O)_2POCl$ (ads) ⟶ $(C_xH_yO)_z$ (ads) + PO_x (ads) + Cl_x (ads)

(3) $(C_xH_yO)_z$ (ads) + PO_x (ads) + Cl_x (ads) [<100°C]

(4) PO_x (ads) + Cl_x (ads) [<125°C]

(5) PO_x (ads) [<150°C]

(ads) – adsorbed; (g) – gas reactant/product

Figure 13. Schematic representation of the adsorption (1−2) and desorption (3−5) with annealing steps (100, 125, 150 °C) of DMCP ($(CH_3O)_2P(O)Cl$) on ZIF-8.

of diffraction peaks and an overall shift to the lower 2θ is observed. This phenomenon illustrates that the adsorbed DMCP molecules and decomposition products are liberated from the ZIF framework and the occupied sites become void (Figure S20, SI). Visual examination of the diffraction data shows that the crystallinity and structural stability of the ZIF-8 structure is maintained after the treatment process; the peaks that appear as new in the treated ZIF-8 are indeed present in the pristine sample with much lower intensity (Figure S21, SI). The nonlinear changes to the diffraction patterns in the higher 2θ angles indicate that the DMCP adsorption/desorption process is not homogeneous, likely due to the different interactions of DMCP with the crystal planes and pore cavities. When tracking the DMCP adsorption/desorption process, we notice that the cell volume shrinks under DMCP adsorption, and then rapidly increases close to the initial volume of pre-exposed ZIF-8 upon regeneration treatment (Figure 14 and

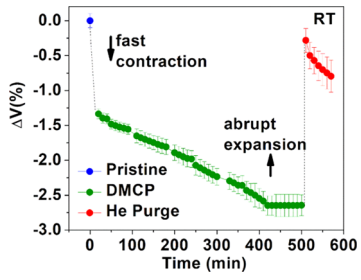

Figure 14. Room temperature structural evolution with an evaluation of regeneration as the progression of cell volume of ZIF-8 from under (1) helium (He) purge, (2) DMCP dosing, and (3) helium (He) purge after heating at 150 °C following the DMCP dosing experiment.

Table S6). Furthermore, when comparing the DMCP-loaded ZIF-8 with the regenerated ZIF-8, there is almost a 2% increase in cell volume after the system is purged with helium, which demonstrates that the majority of adsorbed DMCP molecules are liberated during this process. This increase in cell volume close to the starting point signifies that ZIF-8 is almost 90% regenerated after this adsorption/desorption process (Table S6, SI). Overall, we have shown the successful regeneration of ZIF-8 by flushing with helium at 150 °C after prolonged exposure to DMCP.

In conclusion, by performing a multimodal analysis, we shed light on the reaction mechanism for DMCP decomposition on ZIF-8. The methyl groups provide the necessary hydrophobicity to allow for optimal DMCP adsorption.[36] As we saw from infrared spectroscopy results, the linker molecules are direct sites for DMCP reaction and decomposition. The interaction of decomposition products with nitrogen moieties on the linker facilitates coordination of bound products. The time-resolved analysis of XRD and PDF data reveals that the pore volume is quickly filled and the nitrogen and carbon atoms of the imidazole partake in the reaction. X-ray absorption spectroscopy, X-ray photoelectron spectroscopy, and infrared spectroscopy data proved that metal ion sites are also involved in the reaction with DMCP. The detailed investigation of the interactions of DMCP with the ZIF-8 system in this work reveals that the material's chemical, thermal, and/or structural stability is not irreversibly affected by DMCP binding and can be regenerated by helium treatment at high temperatures.

SUMMARY

In summary, we have investigated the interactions between zeolitic-based imidazolate, ZIF-8, with a nerve agent simulant, DMCP, that result in the decomposition of DMCP and regeneration of the materials with heating. A combination of spectroscopy, scattering, and imaging methods, some of them performed under *in situ* conditions, provided evidence for the adsorption and decomposition of DMCP and elucidated corresponding changes in the ZIF-8 structure. Information we obtained by combining data from different inputs allowed us to propose that interactions of the linker units with DMCP occur through the imidazole nitrogen. Together, these complimentary tools have provided strong evidence of the reaction of phosphonate moiety with Zn^{2+} ions. The time-resolved analysis of PXRD and PDF data reveals that the pore volume is rapidly filled. Based on the differential atomic PDF analysis, we conclude that DMCP initially interacts with the ZIF-8 surface and first adsorbs into the pore window, and then into the pore cavity. Furthermore, we conclude that the adsorption of DMCP into the pore window is slower than in the pore cavity. Using an *in situ* time-resolved analysis, we have shown that the ZIF-8 material can be regenerated with heating with the release of DMCP and DMCP decomposition products. Our study sets the stage for performing a detailed investigation of GB interaction with ZIF-8 and has demonstrated that ZIF-8 can be a useful platform for studying the uptake and decomposition of CWAs and their simulants in real battlefield conditions.

ASSOCIATED CONTENT

Supporting Information

The Supporting Information is available free of charge at https://pubs.acs.org/doi/10.1021/acsami.0c12985.

Additional figures and tables as detailed in the text and include: jar-in-jar setup, chemical structures of sarin and simulants, N_2 isotherms, thermograms, FT-IR, Raman, DRIFTS, and XAFS spectra, results of LeBail fit, PXRD and PDF patterns as well as tables with assigned IR bands and unit cell parameters for ZIF-8 under helium,

https://dx.doi.org/10.1021/acsami.0c12985
ACS Appl. Mater. Interfaces 2020, 12, 58326−58338

under DMCP exposure, and for the regenerated ZIF-8 (PDF)

AUTHOR INFORMATION

Corresponding Author

Anatoly I. Frenkel − *Department of Materials Science and Chemical Engineering, Stony Brook University, Stony Brook, New York 11794, United States; Chemistry Division, Brookhaven National Laboratory, Upton, New York 11973, United States;* orcid.org/0000-0002-5451-1207; Email: anatoly.frenkel@stonybrook.edu

Authors

Amani M. Ebrahim − *Department of Materials Science and Chemical Engineering, Stony Brook University, Stony Brook, New York 11794, United States;* orcid.org/0000-0001-9979-2586

Anna M. Plonka − *Department of Materials Science and Chemical Engineering, Stony Brook University, Stony Brook, New York 11794, United States;* orcid.org/0000-0003-2606-0477

Ning Rui − *Chemistry Division, Brookhaven National Laboratory, Upton, New York 11973, United States*

Sooyeon Hwang − *Center for Functional Nanomaterials, Electron Microscopy Group, Brookhaven National Laboratory, Upton, New York 11973, United States;* orcid.org/0000-0001-5606-6728

Wesley O. Gordon − *U.S. Army Combat Capabilities Development Command Chemical Biological Center, Aberdeen Proving Ground, Maryland 21010, United States;* orcid.org/0000-0001-7766-4102

Alex Balboa − *U.S. Army Combat Capabilities Development Command Chemical Biological Center, Aberdeen Proving Ground, Maryland 21010, United States*

Sanjaya D. Senanayake − *Chemistry Division, Brookhaven National Laboratory, Upton, New York 11973, United States;* orcid.org/0000-0003-3991-4232

Complete contact information is available at: https://pubs.acs.org/10.1021/acsami.0c12985

Notes

The authors declare no competing financial interest.

ACKNOWLEDGMENTS

This work is supported by the U.S. Army Research Laboratory and the U.S. Army Research Office under grant number W911NF-15-2-0107. We thank the Defense Threat Reduction Agency for support under program CB3587. The N_2 isotherm measurements were supported by Joint Science and Technology Office for Chemical and Biological Defense (JSTO-CBD) under project BA13PHM210. Reaction tests and DRIFTS measurements at Brookhaven National Laboratory's Chemistry Division were made possible due to the Laboratory Directed Research and Development Program (LDRD 20-040) support to A.I.F. This research used beamlines 7-BM (QAS), 8-BM (TES), and 28-ID-2 (XPD) of the National Synchrotron Light Source II, a U.S. DOE Office of Science User Facility operated for the DOE Office of Science by Brookhaven National Laboratory under Contract no. DE-SC0012704. This research used resources of the Center for Functional Nanomaterials, which is a U.S. DOE Office of Science Facility, at Brookhaven National Laboratory under Contract no. DE-SC0012704. We thank Dr. Sergio J. Garibay at CBC for the N_2 isotherm measurements.

REFERENCES

(1) Bajgar, J. Chemical Weapon. In *Nerve Agents Poisoning and Its Treatment in Schematic Figures and Tables*; Bajgar, J., Ed.; Elsevier: Oxford, 2012; Chapter 2, pp 3−4.

(2) Geoghegan, J.; Tong, J. L. T. Chemical Warfare Agents. *Cont. Ed. Anaesth., Crit. Care Pain* **2006**, *6*, 230−234.

(3) Bajgar, J.; Fusek, J.; Kassa, J.; Jun, D.; Kuca, K.; Hajek, P. An Attempt to Assess Functionally Minimal Acetylcholinesterase Activity Necessary for Survival of Rats Intoxicated with Nerve Agents. *Chem.-Biol. Interact.* **2008**, *175*, 281−285.

(4) Ganesan, K.; Raza, S. K.; Vijayaraghavan, R. Chemical Warfare Agents. *J. Pharm. BioAllied Sci.* **2010**, *2*, 166−178.

(5) Singer, B. C.; Hodgson, A. T.; Destaillats, H.; Hotchi, T.; Revzan, K. L.; Sextro, R. G. Indoor Sorption of Surrogates for Sarin and Related Nerve Agents. *Environ. Sci. Technol.* **2005**, *39*, 3203−3214.

(6) Lagasse, B. A. Decomposition of Chemical Warfare Agent Simulants Utilizing Pyrolyzed Cotton Balls as Wicks. Master Thesis, Clemson University: South Carolina, 2020.

(7) Tsyshevsky, R.; Head, A. R.; Trotochaud, L.; Bluhm, H.; Kuklja, M. M. Mechanisms of Degradation of Toxic Nerve Agents: Quantum-Chemical Insight into Interactions of Sarin and Soman with Molybdenum Dioxide. *Surf. Sci.* **2020**, *700*, No. 121639.

(8) Wright, A. J.; Main, M. J.; Cooper, N. J.; Blight, B. A.; Holder, S. J. Poly High Internal Phase Emulsion for the Immobilization of Chemical Warfare Agents. *ACS Appl. Mater. Interfaces* **2017**, *9*, 31335−31339.

(9) Sinha Roy, K.; Goud, D. R.; Mazumder, A.; Chandra, B.; Purohit, A. K.; Palit, M.; Dubey, D. K. Triazine-Based Covalent Organic Framework: A Promising Sorbent for Efficient Elimination of the Hydrocarbon Backgrounds of Organic Sample for GC−MS and ^{1}H NMR Analysis of Chemical Weapons Convention Related Compounds. *ACS Appl. Mater. Interfaces* **2019**, *11*, 16027−16039.

(10) Jung, H.; Kim, M.-K.; Lee, J.; Kwon, J. H.; Lee, J. Characterization of the Zirconium Metal-Organic Framework (MOF) UiO-66-NH_2 for the Decomposition of Nerve Agents in Solid-State Conditions Using Phosphorus-31 Solid State-Magic Angle Spinning Nuclear Magnetic Resonance (^{31}P SS-MAS NMR) and Gas Chromatography − Mass Spectrometry (GC-MS). *Anal. Lett.* **2020**, 1−13.

(11) Ma, K.; Islamoglu, T.; Chen, Z.; Li, P.; Wasson, M. C.; Chen, Y.; Wang, Y.; Peterson, G. W.; Xin, J. H.; Farha, O. K. Scalable and Template-Free Aqueous Synthesis of Zirconium-Based Metal−Organic Framework Coating on Textile Fiber. *J. Am. Chem. Soc.* **2019**, *141*, 15626−15633.

(12) Wang, G.; Sharp, C.; Plonka, A. M.; Wang, Q.; Frenkel, A. I.; GuO, W.; Hill, C.; Smith, C.; Kollar, J.; Troya, D.; Morris, J. R. Mechanism and Kinetics for Reaction of the Chemical Warfare Agent Simulant, DMMP(g), with Zirconium(IV) MOFs: An Ultrahigh-Vacuum and DFT Study. *J. Phys. Chem. C* **2017**, *121*, 11261−11272.

(13) Wang, Q.; Chapleski, R. C.; Plonka, A. M.; Gordon, W.; Guo, W.; Nguyen-Phan, T.-D.; Sharp, C.; Marinkovic, N. S.; Senanayake, S. D.; Morris, J. R.; Hill, C. L.; Troya, D.; Frenkel, A. I. Atomic-Level Structural Dynamics of Polyoxoniobates During DMMP Decomposition. *Sci. Rep.* **2017**, *7*, No. 773.

(14) Kaledin, A. L.; Troya, D.; Karwacki, C. J.; Balboa, A.; Gordon, W. O.; Morris, J. R.; Mitchell, M. B.; Frenkel, A. I.; Hill, C. L.; Musaev, D. G. Key Mechanistic Details of Paraoxon Decomposition by Polyoxometalates: Critical Role of Para-Nitro Substitution. *Chem. Phys.* **2019**, *518*, 30−37.

(15) Bromberg, L.; Creasy, W. R.; McGarvey, D. J.; Wilusz, E.; Hatton, T. A. Nucleophilic Polymers and Gels in Hydrolytic Degradation of Chemical Warfare Agents. *ACS Appl. Mater. Interfaces* **2015**, *7*, 22001−22011.

(16) Grissom, T. G.; Plonka, A. M.; Sharp, C.; Ebrahim, A. M.; Tian, Y.; Collins-Wildman, D. L.; Kaledin, A. L.; Siegal, H. J.; Troya, D.; Hill, C. L.; Frenkel, A. I.; Musaev, D. G.; Gordon, W. O.; Karwacki, C. J.; Mitchell, M. B.; Morris, J. R. Metal−Organic Framework- and Polyoxometalate-Based Sorbents for the Uptake and Destruction of Chemical Warfare Agents. *ACS Appl. Mater. Interfaces* **2020**, *12*, 14641−14661.
(17) Islamoglu, T.; Chen, Z.; Wasson, M. C.; Buru, C. T.; Kirlikovali, K. O.; Afrin, U.; Mian, M. R.; Farha, O. K. Metal−Organic Frameworks against Toxic Chemicals. *Chem. Rev.* **2020**, *120*, 8130−8160.
(18) Chen, H.; Snurr, R. Q. Insights into Catalytic Gas-Phase Hydrolysis of Organophosphate Chemical Warfare Agents by MOF-Supported Bimetallic Metal-Oxo Clusters. *ACS Appl. Mater. Interfaces* **2020**, *12*, 14631−14640.
(19) Palomba, J. M.; Harvey, S. P.; Kalaj, M.; Pimentel, B. R.; DeCoste, J. B.; Peterson, G. W.; Cohen, S. M. High-Throughput Screening of MOFs for Breakdown of V-Series Nerve Agents. *ACS Appl. Mater. Interfaces* **2020**, *12*, 14672−14677.
(20) Kirlikovali, K. O.; Chen, Z.; Islamoglu, T.; Hupp, J. T.; Farha, O. K. Zirconium-Based Metal−Organic Frameworks for the Catalytic Hydrolysis of Organophosphorus Nerve Agents. *ACS Appl. Mater. Interfaces* **2020**, *12*, 14702−14720.
(21) Ruffley, J. P.; Goodenough, I.; Luo, T.-Y.; Richard, M.; Borguet, E.; Rosi, N. L.; Johnson, J. K. Design, Synthesis, and Characterization of Metal−Organic Frameworks for Enhanced Sorption of Chemical Warfare Agent Simulants. *J. Phys. Chem. C* **2019**, *123*, 19748−19758.
(22) Bobbitt, N. S.; Mendonca, M. L.; Howarth, A. J.; Islamoglu, T.; Hupp, J. T.; Farha, O. K.; Snurr, R. Q. Metal−Organic Frameworks for the Removal of Toxic Industrial Chemicals and Chemical Warfare Agents. *Chem. Soc. Rev.* **2017**, *46*, 3357−3385.
(23) Mondloch, J. E.; Katz, M. J.; Isley, W. C., III; Ghosh, P.; Liao, P.; Bury, W.; Wagner, G. W.; Hall, M. G.; DeCoste, J. B.; Peterson, G. W.; Snurr, R. Q.; Cramer, C. J.; Hupp, J. T.; Farha, O. K. Destruction of Chemical Warfare Agents Using Metal−Organic Frameworks. *Nat. Mater.* **2015**, *14*, 512−516.
(24) Agrawal, M.; Boulfelfel, S. E.; Sava Gallis, D. F.; Greathouse, J. A.; Sholl, D. S. Determining Diffusion Coefficients of Chemical Warfare Agents in Metal−Organic Frameworks. *J. Phys. Chem. Lett.* **2019**, *10*, 7823−7830.
(25) Kalinovskyy, Y.; Wright, A. J.; Hiscock, J. R.; Watts, T. D.; Williams, R. L.; Cooper, N. J.; Main, M. J.; Holder, S. J.; Blight, B. A. Swell and Destroy: A Metal−Organic Framework-Containing Polymer Sponge That Immobilizes and Catalytically Degrades Nerve Agents. *ACS Appl. Mater. Interfaces* **2020**, *12*, 8634−8641.
(26) Yao, A.; Jiao, X.; Chen, D.; Li, C. Bio-Inspired Polydopamine-Mediated Zr-MOF Fabrics for Solar Photothermal-Driven Instantaneous Detoxification of Chemical Warfare Agent Simulants. *ACS Appl. Mater. Interfaces* **2020**, *12*, 18437−18445.
(27) Phan, A.; Doonan, C. J.; Uribe-Romo, F. J.; Knobler, C. B.; O'Keeffe, M.; Yaghi, O. M. Synthesis, Structure, and Carbon Dioxide Capture Properties of Zeolitic Imidazolate Frameworks. *Acc. Chem. Res.* **2010**, *43*, 58−67.
(28) Park, K. S.; Ni, Z.; Côté, A. P.; Choi, J. Y.; Huang, R.; Uribe-Romo, F. J.; Chae, H. K.; O'Keeffe, M.; Yaghi, O. M. Exceptional Chemical and Thermal Stability of Zeolitic Imidazolate Frameworks. *Proc. Natl. Acad. Sci. U.S.A.* **2006**, *103*, 10186−10191.
(29) Pérez-Pellitero, J.; Amrouche, H.; Siperstein, F. R.; Pirngruber, G.; Nieto-Draghi, C.; Chaplais, G.; Simon-Masseron, A.; Bazer-Bachi, D.; Peralta, D.; Bats, N. Adsorption of CO_2, CH_4, and N_2 on Zeolitic Imidazolate Frameworks: Experiments and Simulations. *Chem. − Eur. J.* **2010**, *16*, 1560−1571.
(30) Moggach, S. A.; Bennett, T. D.; Cheetham, A. K. The Effect of Pressure on ZIF-8: Increasing Pore Size with Pressure and the Formation of a High-Pressure Phase at 1.47 GPa. *Angew. Chem., Int. Ed.* **2009**, *48*, 7087−7089.
(31) Fairen-Jimenez, D.; Galvelis, R.; Torrisi, A.; Gellan, A. D.; Wharmby, M. T.; Wright, P. A.; Mellot-Draznieks, C.; Düren, T. Flexibility and Swing Effect on the Adsorption of Energy-Related Gases on ZIF-8: Combined Experimental and Simulation Study. *Dalton Trans.* **2012**, *41*, 10752−10762.
(32) Hu, Y.; Liu, Z.; Xu, J.; Huang, Y.; Song, Y. Evidence of Pressure Enhanced CO_2 Storage in ZIF-8 Probed by FT-IR Spectroscopy. *J. Am. Chem. Soc.* **2013**, *135*, 9287−9290.
(33) Hobday, C. L.; Woodall, C. H.; Lennox, M. J.; Frost, M.; Kamenev, K.; Düren, T.; Morrison, C. A.; Moggach, S. A. Understanding the Adsorption Process in ZIF-8 Using High Pressure Crystallography and Computational Modelling. *Nat. Commun.* **2018**, *9*, No. 1429.
(34) Ania, C. O.; García-Pérez, E.; Haro, M.; Gutiérrez-Sevillano, J. J.; Valdés-Solís, T.; Parra, J. B.; Calero, S. Understanding Gas-Induced Structural Deformation of ZIF-8. *J. Phys. Chem. Lett.* **2012**, *3*, 1159−1164.
(35) Casco, M. E.; Cheng, Y. Q.; Daemen, L. L.; Fairen-Jimenez, D.; Ramos-Fernández, E. V.; Ramirez-Cuesta, A. J.; Silvestre-Albero, J. Gate-Opening Effect in ZIF-8: The First Experimental Proof Using Inelastic Neutron Scattering. *Chem. Commun.* **2016**, *52*, 3639−3642.
(36) Liu, H.; Guo, P.; Regueira, T.; Wang, Z.; Du, J.; Chen, G. Irreversible Change of the Pore Structure of ZIF-8 in Carbon Dioxide Capture with Water Coexistence. *J. Phys. Chem. C* **2016**, *120*, 13287−13294.
(37) Plonka, A. M.; Grissom, T. G.; Musaev, D. G.; Balboa, A.; Gordon, W. O.; Collins-Wildman, D. L.; Ghose, S. K.; Tian, Y.; Ebrahim, A. M.; Mitchell, M. B.; Hill, C. L.; Morris, J. R.; Frenkel, A. I. Effect of Carbon Dioxide on the Degradation of Chemical Warfare Agent Simulant in the Presence of Zr Metal Organic Framework MOF-808. *Chem. Mater.* **2019**, *31*, 9904−9914.
(38) Sundberg, R. J.; Martin, R. B. Interactions of Histidine and Other Imidazole Derivatives with Transition Metal Ions in Chemical and Biological Systems. *Chem. Rev.* **1974**, *74*, 471−517.
(39) Hu, Q.; Jayasinghe-Arachchige, V. M.; Zuchniarz, J.; Prabhakar, R. Effects of the Metal Ion on the Mechanism of Phosphodiester Hydrolysis Catalyzed by Metal-Cyclen Complexes. *Front. Chem.* **2019**, *7*, 1−14.
(40) Zagórowska, I.; Kuusela, S.; Lönnberg, H. Metal Ion-Dependent Hydrolysis of RNA Phosphodiester Bonds within Hairpin Loops. A Comparative Kinetic Study on Chimeric Ribo/2′-O-Methylribo Oligonucleotides. *Nucleic Acids Res.* **1998**, *26*, 3392−3396.
(41) Green, H.; Day, A. R. The Tautomeric Character of the Imidazole Ring. *J. Am. Chem. Soc.* **1942**, *64*, 1167−1173.
(42) Zhao, J.; Peng, Q.; Wang, Z.; Xu, W.; Xiao, H.; Wu, Q.; Sun, H.-L.; Ma, F.; Zhao, J.; Sun, C.-J.; Zhao, J.; Li, J. Proton Mediated Spin State Transition of Cobalt Heme Analogs. *Nat. Commun.* **2019**, *10*, No. 2303.
(43) Lambert, F.; Policar, C.; Durot, S.; Cesario, M.; Yuwei, L.; Korri-Youssoufi, H.; Keita, B.; Nadjo, L. Imidazole and Imidazolate Iron Complexes: On the Way for Tuning 3D-Structural Characteristics and Reactivity. Redox Interconversions Controlled by Protonation State. *Inorg. Chem.* **2004**, *43*, 4178−4188.
(44) Lenarcik, B.; Ojczenasz, P. The Influence of the Size and Position of the Alkyl Groups in Alkylimidazole Molecules on Their Acid-Base Properties. *J. Heterocycl. Chem.* **2002**, *39*, 287−290.
(45) Barszcz, B.; Kulig, J. Comparison of the Complexing Processes of 1-Butyl-2-Hydroxymethylimidazole and 1-Butyl-2-Methylimidazole in Aqueous Solution. *J. Chem. Soc., Dalton Trans.* **1993**, 1559−1562.
(46) Son, Y.-R.; Ryu, S. G.; Kim, H. S. Rapid Adsorption and Removal of Sulfur Mustard with Zeolitic Imidazolate Frameworks ZIF-8 and ZIF-67. *Microporous Mesoporous Mater.* **2020**, *293*, No. 109819.
(47) Du, M.; Li, L.; Li, M.; Si, R. Adsorption Mechanism on Metal Organic Frameworks of Cu-BTC, Fe-BTC and ZIF-8 for CO_2 Capture Investigated by X-Ray Absorption Fine Structure. *RSC Adv.* **2016**, *6*, 62705−62716.
(48) Sava, D. F.; Rodriguez, M. A.; Chapman, K. W.; Chupas, P. J.; Greathouse, J. A.; Crozier, P. S.; Nenoff, T. M. Capture of Volatile Iodine, a Gaseous Fission Product, by Zeolitic Imidazolate Framework-8. *J. Am. Chem. Soc.* **2011**, *133*, 12398−12401.

https://dx.doi.org/10.1021/acsami.0c12985
ACS Appl. Mater. Interfaces 2020, 12, 58326−58338

(49) Hughes, J. T.; Sava, D. F.; Nenoff, T. M.; Navrotsky, A. Thermochemical Evidence for Strong Iodine Chemisorption by ZIF-8. *J. Am. Chem. Soc.* **2013**, *135*, 16256−16259.
(50) Zheng, B.; Wang, L. L.; Du, L.; Pan, Y.; Lai, Z.; Huang, K. W.; Du, H. L. Diffusion as a Function of Guest Molecule Length and Functionalization in Flexible Metal−Organic Frameworks. *Mater. Horiz.* **2016**, *3*, 355−361.
(51) Ebrahimi, A.; Nassireslami, E.; Zibaseresht, R.; Mohammadsalehi, M. Ultra-Fast Catalytic Detoxification of Organophosphates by Nano-Zeolitic Imidazolate Frameworks. *Mol. Catal.* **2020**, *490*, No. 110965.
(52) Ebrahim, A. M.; Plonka, A. M.; Tian, Y.; Senanayake, S. D.; Gordon, W. O.; Balboa, A.; Wang, H.; Collins-Wildman, D. L.; Hill, C. L.; Musaev, D. G.; Morris, J. R.; Troya, D.; Frenkel, A. I. Multimodal Characterization of Materials and Decontamination Processes for Chemical Warfare Protection. *ACS Appl. Mater. Interfaces* **2020**, *12*, 14721−14738.
(53) Tian, Y.; Plonka, A. M.; Ebrahim, A. M.; Palomino, R. M.; Senanayake, S. D.; Balboa, A.; Gordon, W. O.; Troya, D.; Musaev, D. G.; Morris, J. R.; Mitchell, M. B.; Collins-Wildman, D. L.; Hill, C. L.; Frenkel, A. I. Correlated Multimodal Approach Reveals Key Details of Nerve-Agent Decomposition by Single-Site Zr-Based Polyoxometalates. *J. Phys. Chem. Lett.* **2019**, *10*, 2295−2299.
(54) Ravel, B.; Newville, A. M. Athena, Artemis, Hephaestus: Data Analysis for X-Ray Absorption Spectroscopy Using IFEFFIT. *J. Synchrotron Radiat.* **2005**, *12*, 537−541.
(55) Hammersley, A. P. Fit2D: A Multi-Purpose Data Reduction, Analysis and Visualization Program. *J. Appl. Crystallogr.* **2016**, *49*, 646−652.
(56) Toby, H. B.; Von Dreele, R. B. GSAS-II: The Genesis of a Modern Open-Source All Purpose Crystallography Software Package. *J. Appl. Crystallogr.* **2013**, *46*, 544−549.
(57) Farrow, C. L.; Juhas, P.; Liu, J. W.; Bryndin, D.; Božin, E. S.; Bloch, J.; Proffen, T.; Billinge, S. J. L. PDFfit2 and PDFgui: Computer Programs for Studying Nanostructure in Crystals. *J. Phys.: Condens. Matter* **2007**, *19*, No. 335219.
(58) Adhikari, P.; Xiong, M.; Li, N.; Zhao, X.; Rulis, P.; Ching, W.-Y. Structure and Electronic Properties of a Continous Random Network Model of an Amorphous Zeolitic Imidazolate Framework (a-ZIF). *J. Phys. Chem. C.* **2016**, *120*, 15362−15368.
(59) Terban, M. W.; Banerjee, D.; Ghose, S.; Measani, B.; Shukla, A.; Legg, B. A.; Zhou, Y.; Zhu, Z.; Sushko, M. L.; De Yoreo, J. J.; Liu, J.; Thallapally, P. K.; Billinge, S. J. L. Early Stage Structural Development of Prototypical Zeolitic Imidazolate Framework (ZIF) in Solution. *Nanoscale* **2018**, *10*, 4291−4300.
(60) Longley, L.; Collins, S. M.; Li, S.; Smales, G. J.; Erucar, I.; Qiao, A.; Hou, J.; Doherty, C. M.; Thornton, A. W.; Hill, A. J.; Yu, X.; Terrill, N. J.; Smith, A. J.; Cohen, S. M.; Midgley, P. A.; Keen, D. A.; Telfer, S. D.; Bennett, T. D. Flux Melting of Metal−Organic Frameworks. *Chem. Sci.* **2019**, *10*, 3592−3601.
(61) Cao, S.; Bennett, T. D.; Keen, D. A.; Goodwin, A. L.; Cheetham, A. K. Amorphization of the Prototypical Zeolitic Imidazolate Framework ZIF-8 by Ball-Milling. *Chem. Commun.* **2012**, *48*, 7805−7807.
(62) Kumari, G.; Jayaramulu, K.; Maji, T. K.; Narayana, C. Temperature Induced Structural Transformations and Gas Adsorption in the Zeolitic Imidazolate Framework ZIF-8: A Raman Study. *J. Phys. Chem. A* **2013**, *117*, 11006−11012.
(63) Eum, K.; Jayachandrababu, J. C.; Rashidi, F.; Zhang, K.; Leisen, J.; Graham, S.; Lively, R. P.; Chance, R. R.; Sholl, D. S.; Jones, C. W.; Nair, S. Highly Tunable Molecular Sieving and Adsorption Properties of Mixed-Linker Zeolitic Imidazolate Frameworks. *J. Am. Chem. Soc.* **2015**, *137*, 4191−4197.
(64) Ettlinger, R.; Moreno, N.; Volkmer, D.; Kerl, K.; Bunzen, H. Zeolitic Imidazolate Framework-8 as pH-Sensitive Nanocarrier for "Arsenic Trioxide" Drug Delivery. *Chem. − Eur. J.* **2019**, *25*, 13189−13196.
(65) Florent, M.; Giannakoudakis, D. A.; Wallace, R.; Bandosz, T. J. Carbon Textiles Modified with Copper-Based Reactive Adsorbents as Efficient Media for Detoxification of Chemical Warfare Agents. *ACS Appl. Mater. Interfaces* **2017**, *9*, 26965−26973.
(66) Balow, R. B.; Lundin, J. G.; Daniels, G. C.; Gordon, W. O.; McEntee, M.; Peterson, G. W.; Wynne, J. H.; Pehrsson, P. E. Environmental Effects on Zirconium Hydroxide Nanoparticles and Chemical Warfare Agent Decomposition: Implications of Atmospheric Water and Carbon Dioxide. *ACS Appl. Mater. Interfaces* **2017**, *9*, 39747−39757.
(67) Velásquez-Hernández, M. D. J.; Ricco, R.; Carraro, F.; Limpoco, F. T.; Linares-Moreau, M.; Leitner, E.; Wiltsche, H.; Rattenberger, J.; Schröttner, H.; Frühwirt, P.; Stadler, E. M.; Gescheidt, G.; Amenitsch, H.; Donnan, C. J.; Falcaro, P. Degradation of ZIF-8 in Phosphate Buffered Saline Media. *CrystEngComm* **2019**, *21*, 4538−4544.
(68) Liu, Z.; Wu, A.; Yan, H.; Su, D.; Jin, C.; Guo, H.; Wang, L.; Tian, C. An Effective "Precursor-Transformation" Route toward High-Yield Synthesis of ZIF-8 Tubes. *Chem. Commun.* **2020**, *56*, 2913−2916.
(69) Wilmsmeyer, A. R.; Gordon, W. O.; Davis, E. D.; Troya, D.; Mantooth, B. A.; Lalain, T. A.; Morris, J. R. Infrared Spectra and Binding Energies of Chemical Warfare Nerve Agent Simulants on the Surface of Amorphous Silica. *J. Phys. Chem. C* **2013**, *117*, 15685−15697.
(70) Wilmsmeyer, A. R.; Uzarski, J.; Barrie, P. J.; Morris, J. R. Interactions and Binding Energies of Dimethyl Methylphosphonate and Dimethyl Chlorophosphate with Amorphous Silica. *Langmuir* **2012**, *28*, 10962−10967.

https://dx.doi.org/10.1021/acsami.0c12985
ACS Appl. Mater. Interfaces 2020, 12, 58326−58338